Soft Matter

Foam Film Stratification, Viscosity, and Small-Angle X-ray Scattering of Micellar SDS Solutions over an Extended Concentration Range (1< c/CMC < 75)

Journal:	*Soft Matter*
Manuscript ID	SM-ART-08-2023-001069.R1
Article Type:	Paper
Date Submitted by the Author:	17-Dec-2023
Complete List of Authors:	Ochoa, Chrystian; University of Illinois at Chicago, Chemical Engineering Gao, Shang; University of California Los Angeles, Department of Chemical and Biomolecular Engineering Xu, Chenxian; University of Illinois at Chicago Srivastava, Samanvaya; UCLA, Chemical and Biomolecular Engineering Sharma, Vivek; University of Illinois at Chicago, Chemical Engineering

Foam Film Stratification, Viscosity, and Small-Angle X-ray Scattering of Micellar SDS Solutions over an Extended Concentration Range (1< c/CMC < 75)

Chrystian Ochoa[1], Shang Gao[2], Chenxian Xu[1], Samanvaya Srivastava[2,3,4,5]*, and Vivek Sharma[1]*

[1]Department of Chemical Engineering, University of Illinois Chicago, 929 W Taylor St, Chicago, IL 60607, USA
[2]Department of Chemical and Biomolecular Engineering, University of California, Los Angeles, Los Angeles, CA 90095, USA
[3]California NanoSystems Institute, University of California, Los Angeles, Los Angeles, CA 90095, USA
[4]Center for Biological Physics, University of California, Los Angeles, Los Angeles, CA 90095, USA
[5]Institute for Carbon Management, University of California, Los Angeles, Los Angeles, CA 90095, USA
*Address correspondence to: viveks@uic.edu or samsri@ucla.edu
Submitted on August 13, 2023, Revised December 8, 2023

ABSTRACT

Ultrathin foam films (thickness, h < 100 nm) containing micelles undergo drainage *via* stratification manifested as coexisting thick-thin flat regions, nanoscopic non-flat topography, and the stepwise decrease in film thickness that yields a characteristic step-size. Most studies characterize the variation in step size and stratification kinetics in micellar foam films in a limited concentration range c/CMC < 12.5 (c < 100 mM). Likewise, most scattering studies characterize micelle dimensions, intermicellar distance, and volume fraction in bulk aqueous SDS solutions in this limited concentration range. In this contribution, we show drainage via stratification can be observed for concentrations up to c/CMC < 75 (c < 600 mM). Understanding the role of micelles on the stratification behavior of draining films with sodium dodecyl sulfate (SDS) concentration 10 mM ≤ c_{SDS} ≤ 600 mM is essential for molecular engineering, consumer product formulations, and controlling foaming in industrial processes. Here, we visualize and analyze nanoscopic thickness variations and transitions in stratifying foam films using Interferometry Digital Imaging Optical Microscopy (IDIOM) protocols and compare these parameters to micelle dimension, micelle volume fraction, and intermicellar distance obtained from small angle X-ray scattering studies. Even though the volume fraction increases and approaches 25% at c = 600 mM, the solution viscosity only increases by a factor of four compared to the solvent, consistent with the findings from both stratification and scattering studies. These comparisons allow us to explore the effect of micelle size, morphology, and intermicellar interactions on supramolecular oscillatory structural disjoining pressure, which influences the stratification behavior of draining foam films containing micelles under confinement.

INTRODUCTION

Sodium dodecyl sulfate (SDS), or sodium lauryl sulfate, is an anionic head-tail surfactant containing a twelve-carbon alkyl chain as the hydrophobic tail. In aqueous solutions, SDS unimers disassociate into sodium ions and a negatively charged dodecyl sulfate group), with the charged sulfate group covalently attached to the alkyl tail. The rapid adsorption of SDS to air-water interface reduces surface tension, σ from $\sigma = 72$ mNm^{-1} to nearly half, thus reducing capillary pressure, $P_c = \sigma C$ for fixed curvature, C by half, and improving wettability, foamability, and foam stability.[1-3] In solution, SDS forms self-assembled spherical aggregates called micelles above critical micelle concentration, CMC. Though the reported values vary slightly with the measurement technique used,[2-8] surface tension-concentration curve yields CMC ≈ 8.2 mM or 0.24 wt.% (for the SDS used in our studies[9]). The nearly spherical micelles with hydrophobic cores solubilize organic, hydrophobic chemicals, providing SDS with detergent properties. SDS is the preferred ingredient of many cleaning formulations in laundry, dishwashing, and surface care, with significant applications in coatings and cosmetics. In the biomedical industry, SDS is used for lysing cells for RNA and DNA extraction and denaturing proteins for gel electrophoresis. H. Bertsch of T. Bóhme, A.-G. and W. Schrauth of Deutsche Hydrierwerke A.-G., who introduced SDS in the early 1930s as a detergent[10, 11] might not have anticipated the diverse applications and economic impact (over half a billion dollars a year). However, increased concerns about the impact of human-made chemicals on the environment, bio-organisms, and human health are driving research into alternative surfactants,[12, 13] and imitable properties and stability of SDS foams. Foam films formed with micellar SDS solutions undergo delayed drainage via stratification, manifested as stepwise thinning and coexisting thick-thin regions.[14-22] Most previous studies (including our own)[14-36] focused on a limited concentration range (c/CMC ≤ 12.5) for SDS and likewise for other

surfactants, even though higher concentrations abound in practice, motivating this study, over a substantially expanded concentration range (c/CMC < 75).

Freshly formed foam films and soap bubbles or films, illuminated by white light display iridescence due to the interference of light reflected from the two liquid-air interfaces.[37-40] However, on a decrease in film thickness due to drainage, bright colors give way to progressively darker grays with intensities correlated with their thickness for ultrathin micellar foam films (thickness, h < 100 nm). In reflected light microscopy, the micellar foam films that undergo drainage via stratification exhibit distinct gray shades mapping the coexisting thick-thin flat regions.[9, 14-36, 41-43] Furthermore, the stepwise thinning with constant step-size, Δh is present in thickness-time plots constructed by analyzing average intensity from a region of interest in foam film. This step size equals the thickness difference between the spontaneously formed and expanding flat thinner domains and their flat, thicker surroundings. Capillarity-driven squeeze flow in ultrathin (h < 100 nm) freestanding (foam) and supported (containing one or two solid boundaries) films[1, 44, 45] is influenced by bulk and interfacial rheology[3, 44, 46-48] as well as thickness-dependent disjoining pressure, $\Pi(h)$. Intermolecular and surface forces determine the strength and range of disjoining pressure, $\Pi(h)$ as well as of colloidal interaction forces $F(h)$.[1, 2, 44, 47, 49-51] Intermicellar structuring under confinement and intermicellar interactions contribute a thickness-dependent supramolecular structural oscillatory disjoining pressure, $\Pi_{OS}(h)$ that balances P_c at discretized thickness values forming coexisting thick-thin flat regions that differ by Δh in thickness.[15, 17, 22, 30, 31] In analogy with structural oscillatory forces like solvation forces in simple fluids, the periodicity, λ due to layering and the decay length, ξ due to the diminishing effect of confinement can be incorporated into a phenomenological expression[2, 17, 32, 33, 52-54] for $\Pi_{OS}(h) = A_{eff} \exp\left(-\frac{h}{\xi}\right) \cos\left(-\frac{2\pi h}{\lambda}\right)$. Using an analytical form based on Kralchevsky and

Denkov model,[52] we can estimate the prefactor, $A_{eff}(c) = \rho f(\phi_{eff}) k_B T$ from the knowledge of micelle number density, ρ, thermal energy, $k_B T$ and the Carnahan-Starling compressibility factor, $f(\phi_{eff})$ computed at an effective micellar volume fraction, ϕ_{eff} assuming effective hard spheres formed by combining the Debye length and micelle size.[33, 54] Statistical mechanics approaches like density functional theory allow computation of the confinement-induced structuring leading to inhomogeneous micellar density near walls and $\Pi_{OS}(h)$ or $F(h)$ that are oscillatory, but not exactly sinusoidal and give viscosity estimates slightly lower than bulk value.[25, 53-59]

The Δh values obtained from stratification studies are comparable to the periodicity, λ of the oscillatory structural disjoining pressure, $\Pi_{os}(h)$ measured using thin film balance,[16, 17] and intermicellar distance, d predicted by theory.[55, 56] Several groups postulated $\Delta h \cong d$ by drawing a connection between periodicity, λ of force-distance curves (that emulate $\Pi_{os}(h)$ vs h plots) and interparticle distance, d in nanoparticle dispersions.[26, 27, 54, 60-65] Based on this analogy Anachkov et al.[27] had postulated that the inverse cubic root relationship between step-size, Δh, and concentration of ionic surfactant $\Delta h \sim c^{-1/3}$ is valid for solutions containing spherical micelles/particles up to volume fraction of $\phi = 0.56$. However, this claim has not been tested for surfactant systems for a broad concentration range, and liquid-state models, including the Carnahan-Starling model, are inapplicable for $\phi > 0.55$. Head-tail surfactants display spherical-like micelles only for a limited range of concentration. Rod-like micelles, lamellar structures, and other liquid crystalline phases can form at much higher concentrations.[4, 66-69] Even though a phase diagram for SDS was compiled by Kekicheff[4] in 1988, only a countable few scattering studies describe micelle volume fraction, micelle dimensions, and intermicellar distances[69-73] for c/CMC > 15, and only a couple of higher concentrations solutions were explored to evaluate drainage *via* stratification behavior.[23, 25] We showed recently[20] that the intermicellar distance, d measured by

small-angle x-ray scattering in bulk SDS solutions matches the step-size or $\Delta h \approx d$ in salt-free for foam films for 30 mM $\leq c_{SDS} \leq$ 225 mM (for c/CMC < 30). In these salt-free SDS solutions, the interfacial charge and tension and the shape and size of micelles are nearly unchanged. The cubic root relationship $\Delta h \sim c^{-1/3}$ represents the influence of pairwise intermicellar interactions governed by screened Coloumb interactions and the symmetry-breaking at the interface on the structuring and layering of micelles under confinement. However, we observed that the two relationships: $\Delta h \sim c^{-1/3}$ and $\Delta h \approx d$ are disrupted in salt-added SDS solutions,[33, 34], implying the analogy between particles and micelles breaks down, as salt addition changes the interfacial charge (and potential) and interfacial tension, as well as micellar number density and dimensions.[33, 34]

Typically thickness measurements of stratifying surfactant films are carried out by using a laser as a source of monochromatic light and a photodiode as a detector to measure the average reflected light intensity from a sample spot on the film.[3, 16, 17, 24-29, 42, 43, 46, 74] Such measurements show the stepwise thinning without providing any insights into the nanotopography of the stratifying foam films. We recently pioneered IDIOM (Interferometry Digital Imaging Optical Microscopy) protocols to visualize and analyze the spatiotemporal variation in thickness of the entire foam film, computed using the pixel-wise interference intensity captured by the photosensor array of a digital camera attached to a microscope.[19, 22] The IDIOM protocols facilitate a detailed characterization of the nanoscopic topography of the stratifying foam films, the average step-size, Δh, and the number of stepwise transitions before rupture.[9, 19-22, 30-36] After experimentally characterizing the first thickness maps,[22] we illustrated that the thin film hydrodynamics and thermodynamics lead to observed stratification process[22, 30, 31] and extensively characterized the evolving grayscale (thick-thin) regions due to flat and non-flat nanotopography in stratifying foam

films for a range of surfactant types[9, 20, 36] and salt concentrations[33, 34]. However, the concentrations were limited to the usual range ($1< c/\mathrm{CMC} < 15$).

In this manuscript, we carry out an examination of foam drainage for an extended range of SDS concentrations 10 mM ≤ c_{SDS} ≤ 600 mM ($1 < c/\mathrm{CMC} < 75$) to determine how the progressive increase in SDS concentration influences the drainage process and if stratification is manifested for a broader range of concentrations than reported and examined before. We characterize the nanotopography of stratified foam films using IDIOM protocols and evaluate the concentration-dependent variation in step size, Δh and median number of steps, N_{med}. The variation in topography, Δh, and N_{med} show impact on intermicellar interactions and the amplitude and periodicity of supramolecular oscillatory structural disjoining pressure, Π_{OS} that drives stratification. Furthermore, we characterize changes in micellar volume fraction, micelle shape, and size using SAXS measurements. We characterized concentration-dependent variation in shear viscosity to assess the influence of change in micellar number density, dimensions, and interactions. We compare the concentration-dependent variation of the intermicellar distance in bulk (measured by scattering) to the step size of stratifying foam films to determine the impact of intermicellar interactions and structuring on foam film drainage. Our scattering and stratification studies address unchartered questions regarding the role of changing micelle size, shape, number, and screened charge interactions on stratification, and highlight the limited scope of analogy often drawn between confined particles and micelles in stratifying foam films.

MATERIALS AND METHODS

Aqueous SDS Solutions

Micellar solutions of SDS in the concentration range 10 ≤ c_{SDS} ≤ 600 mM were prepared by dissolving as-received SDS (Sigma-Aldrich Co., St. Louis, MO, L6026, purity > 99.0%) in

deionized water of resistivity 18.2 MΩ·cm). As described in a previous study, the concentration-dependent variation in surface tension of the aqueous SDS solutions was measured using maximum bubble pressure tensiometry and pendant drop tensiometry.[75] The σ *vs.* c_{SDS} plot revealed CMC = 8.2 mM, and the absence of any dip near CMC indicates that the as-made solutions are relatively free of impurities. As the adsorption time scale (< 100ms) is much smaller than the drainage time scale (in seconds), dynamic adsorption effects can be ignored. Surface tension above CMC remains unchanged. The shear rheology response of the aqueous SDS solutions was characterized using double gap Couette geometry on an Anton Paar MCR 302 WESP rheometer at 25 ˚C. Steady shear viscosity was measured as a function of shear rate, and as viscosity appears rate-independent, a single number is used for describing the shear viscosity at concentrations explored in this study.

Foam Films of Aqueous SDS Solutions

Each horizontal foam film of micellar SDS solutions was created by pumping a finite fluid volume into a Scheludko-type cell (internal diameter, d_c = 1.6 mm). The cell is enclosed in a closed environment that includes a container with an aqueous surfactant solution to create a saturated atmosphere and minimize foam film evaporation effects that can affect stratification behavior. Using a syringe pump to control the rate of flow from a syringe, the surfactant solution is passed through a side-arm connected to an aperture on the side of the horizontal Scheludko-like cell (see Figure 1a) until a biconcave drop forms in the cell. The sidearm connected to a syringe pump was later used to slowly withdraw the fluid until the last vestiges of interference colors disappeared and a plane-parallel, ultrathin liquid film formed (with initial thickness ~ 100nm). The syringe pump is switched off for the remainder of the experiment to allow drainage under the local balance of stresses into a surrounding meniscus that emulates the Plateau border around a single foam film.

The Laplace pressure inside the meniscus depends on cell diameter, d_c and film diameter, d_f ~300 μm and is estimated using $P_c \approx 4\sigma d_c / \left(d_c^2 - d_f^2\right)$ to be $P_c \approx 90$ Pa for the experiments described in this study.

Small Angle X-ray Scattering

Small-angle X-ray scattering (SAXS) measurements were performed at beamline 12-ID-B at the Advanced Photon Source (APS) in Argonne National Laboratory. The solutions were placed in 2 mm thin-walled quartz capillary tubes (Charles Supper Company, Inc.) and were equilibrated at room temperature for at least 24 hours before the scattering experiments. The one-dimensional scattering intensity, $I(q)$ was obtained from the azimuthal averaging of the two-dimensional scattering speckle data. Scattering from the solvent and capillary background was subtracted to obtain $I(q)$ from the SDS self-assemblies in the solution as a function of the wave vector $q = \frac{4\pi \sin\theta}{\lambda}$ in the q = 0.3 – 3 nm^{-1} range. Here, 2θ is the angle between the incident beam and the detector, and λ is the wavelength of the X-ray radiation. As the intensity, $I(q)$, profile depends on the structure factor, $S(q)$, set by intermicellar interference, and the form factor, $P(q)$, set by intramicellar interference, the structural and micelle characteristics are obtained by fitting the product $\phi P(q)S(q)$ to the experimental $I(q)$ data using custom-written scripts in MATLAB.[20, 34]

Drainage via Stratification Studies using IDIOM Protocols

Foam film formed in the Scheludko-cell is illuminated by white light emanating from a Fiilex P360EX portable LED 4000K color light source. High-resolution images in m-RAW format are obtained using a FASTCAM Mini UX100 high-speed color camera attached to a precision microscope lens system (Navitar Zoom 6000, with added 10x microscope objective) that captures the reflected interference intensities from the foam film. The in-built camera photo-sensor array

captures the pixel-wise, spatio-temporal variation of the interference intensity $I(x,y,\lambda,t)$. Each pixel in the color image can be read as a combination of red (λ = 630 nm), green (λ = 546 nm), and blue (λ = 470 nm) reflected light intensities with dynamic range = 0-4095 (for images in RAW format, with a 12-bit depth camera).

For each pixel and each color channel, the interference intensity, $I = I(x, y, \lambda, t)$ was converted into apparent film thickness, $h(x,y, t)$, by using the interferometry equation[40, 46]:

$$h = \left(\frac{\lambda}{2n\pi}\right)\arcsin\left(\sqrt{\frac{\Delta}{1+4R(1-\Delta)/(1-R)^2}}\right) \quad (1)$$

Here, the normalized intensity, $\Delta = (I - I_{\min})/(I_{\max} - I_{\min})$ computes the intensity values normalized by using the maxima and minima values of interference intensities, $I_{\max}$ and $I_{\min}$. The reflectivity $R = (n-1)^2/(n+1)^2$ depends on the refractive index, n and the value for water (n = 1.33) is used for all solutions, which gives a measurement of an effective thickness, h. In each pixel, the film thicknesses obtained from three color channels were averaged, though there is an insignificant difference (< 1 nm) between them. Thus, the thickness map of the entire film, $h(x, y, t)$ with a spatial resolution of 0.44 μm/pixel, thickness resolution of ~1nm, and a temporal resolution under a millisecond, could be constructed pixel-by-pixel from the intensity $I(x, y, t)$ obtained with white light illumination and digital filtering. The average intensity of a fixed square region on the film (side length ~11 μm) yielded the thickness-time plots that show a stepwise decrease. The layer thicknesses, h_n were determined as the minimum thickness it reaches a quasi-steady state value, whereas the terminal thickness, h_0 was obtained after the jump. Multiple regions were analyzed to check for consistency and to minimize error. The step-size were averaged through all h_n-h_{n-1}, but the last step h_1-h_0 was excluded as DLVO forces could provide additional contribution to disjoining

pressure.[36] Data points in the Δh and h_0 vs. c_{SDS} plot were obtained from 3-4 distinct experiments with freely draining foam films, and the film topographies at the two air-liquid surfaces are assumed to be similar. The thicknesses separately measured for the three camera color channels agree (< 1 nm difference). The image analysis is completed in MATLAB R2020a with specifically developed codes. The IDIOM protocols facilitate the creation of thickness maps of the foam films with high spatial (thickness < 1 nm, lateral ~ 500 nm) and temporal (~ 20 ms) resolution.[22, 32]

RESULTS AND DISCUSSION

Drainage *via* stratification: characterization of stepwise thinning

Figure 1a shows the schematic of the IDIOM setup used for measuring thickness variations and transitions as a function of time for a plane parallel film (radius ~ 0.35 mm) surrounded by a much thicker meniscus within the Scheludko-like cell (radius = 1.6 mm). Here, the spatiotemporal variation in thickness of the freely draining film is computed using the pixel-wise interference intensity using equation (1). A sequence of four snapshots is included as Figure 1b for micellar foam films formed with c_{SDS} = 200 mM. The emergence of progressively darker grey shades with time in the snapshots shown in Figure 1b indicates that the average film thickness decreased with time. The snapshots show multiple coexisting shades of gray, corresponding to different thickness-dependent interference intensities and, hence, coexisting thick-thin regions. Visualization of thinning foam films reveals that thinner, darker domains spontaneously nucleate and grow**.** The number of domains formed progressively decreases with foam film thickness. For example, the number of domains decreased from 6 to 1 in snapshots included for t = 11.9 s and t = 23.7 s, respectively, in Figure 1b. The thinner, flat domains emerge due to an interplay of capillary pressure and a highly nonlinear, thickness-dependent disjoining pressure. The coexisting flat

regions display quantized thickness differences between them equal to a concentration-dependent step-size.

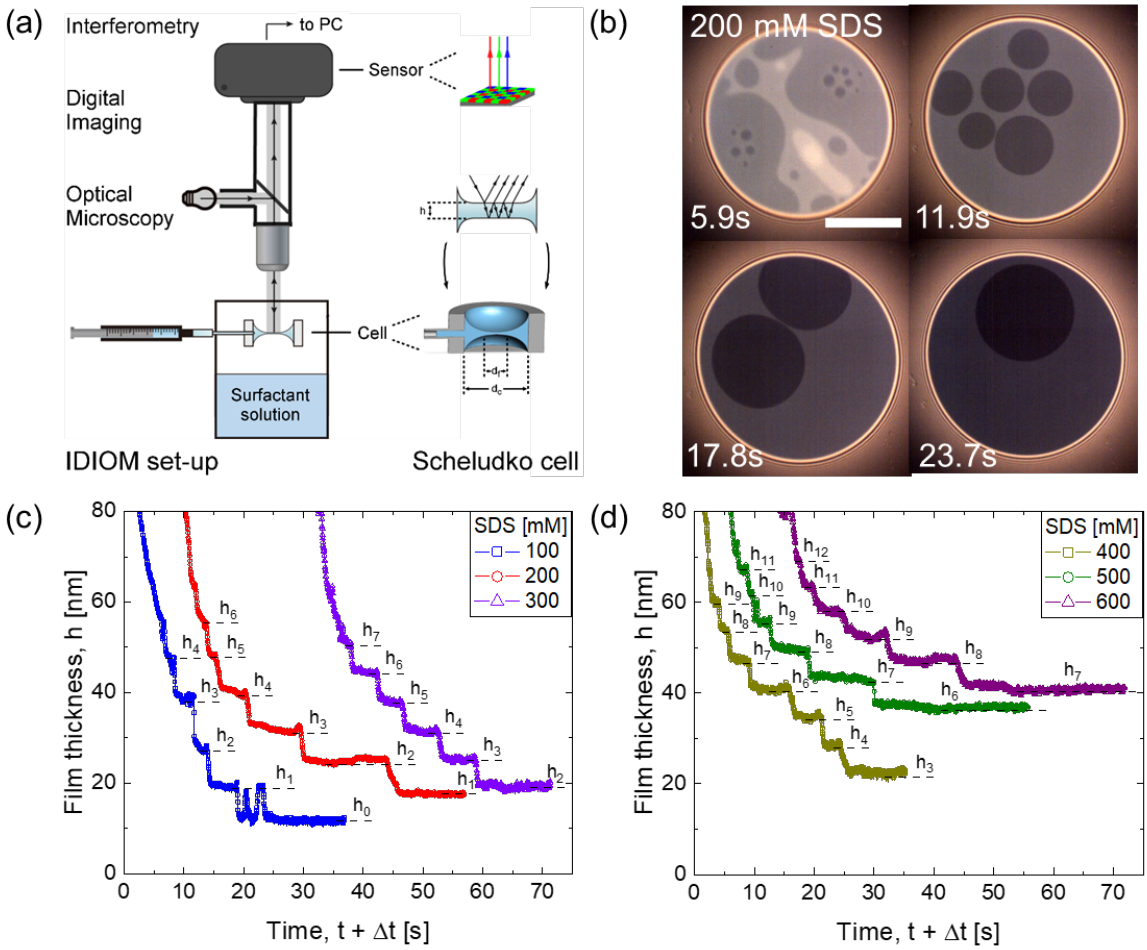

Figure 1. Drainage via stratification studies carried out using IDIOM (Interferometry Digital Imaging Optical Microscopy) protocols to obtain snapshots and thickness evolution plots for stratifying SDS films. (a) Schematic shows the IDIOM setup used for measuring thickness variations and transitions of a circular freely-draining plane-parallel film surrounded by a thicker meniscus, that is created in a Scheludko cell. The spatiotemporal variation in interference intensity captured by the photosensor array of a digital camera is used for obtaining pixelwise thickness measurement. **(b)** Brightness-enhanced snapshots for c_{SDS} = 200 mM film showing progressively dark shades of grey as film drains over time. The scale bar inset corresponds to 100 µm. **(c)** Average thickness-time plots for varying SDS concentration solutions (c_{SDS} = 100, 200, 300 mM), measured using a 10.4-micron-a-side square region show stepwise thinning. Each step separates two successive metastable thicknesses labeled h_{i+1} and h_i. The minimum metastable thickness is h_0 for c_{SDS} = 100 mM, h_1 for c_{SDS} = 200 mM and h_2 for c_{SDS} = 300 mM. Plots have been shifted horizontally for clarity of viewing. **(d)** Average thickness-time plots for relatively high SDS concentration solutions (c_{SDS} = 400, 500, 600 mM) show stepwise thinning, but the minimum metastable thickness observed with the set-up ranges from h_3 to h_7 from c_{SDS} = 400 to 600 mM.

Thickness-time plots shown in Figure 1c-d were obtained by computing average thickness from an average reflected intensity from a 10.4 micron-a-side square region using the interferometry equation (1). The plots show stepwise thinning for micellar SDS foam films, and here each layer thickness h_i is labeled with an index i. Figure 1c shows thickness-time plots for c_{SDS} = 100, 200, and 300 mM. Here the thinnest flat domains corresponded to the terminal (h_0), first step ($h_1 = h_0 + \Delta h$), and second step ($h_2 = h_0 + 2\Delta h$), respectively. These trends are further exacerbated in films with higher c_{SDS}. In Figure 1d, the thickness evolution plots for micellar SDS foam films with c_{SDS} = 400, 500, 600 mM also exhibit stepwise thinning, implying stratification occurs in SDS micellar films up to c_{SDS}/CMC < 75! Here, the minimum thickness observed with fixed Laplace pressure (same cell size and nearly similar film size) is substantially larger than step-size or minimum thicknesses observed for concentrations shown in Figure 1c, and lower concentrations explored in previous studies.[14-27, 30-35, 42, 47] On increasing c_{SDS} = 400 to 600 mM, we observe that (i) the minimum thickness observed increased from h_3 to h_7, (ii) the maximum metastable thickness increased from h_9 to h_{12}, (iii) the metastable thickness h_i decreased; for example, h_9 decreases from 60 to 52 nm, and (iv) the average step-size, again constant for each SDS concentration, decreased from 6.5 to 5.5 nm. However, in contrast to c_{SDS} = 100 to 300 mM trends, the number of layers decreased from 7 to 6 when c_{SDS} increased from 400 mM to 600 mM and can be attributed to the increasing magnitude of oscillatory disjoining pressure with increasing c_{SDS}, leading to a higher energy threshold for nucleation of domains with thinner thicknesses.

Characterization of nanotopography in stratifying films

We visualized and analyzed the flat and non-flat nanoscopic topography of stratifying foam films using IDIOM protocols, as illustrated in Figure 2. Each row shows a series of grayscale snapshots for c_{SDS} = 100, 300, and 600 mM, respectively. Also included are two thickness maps

for each concentration. In row 1, the maps correspond to Figures 2c and 2e, whereas Figures 2j and 2l, and Figures 2q and 2s, respectively, are selected for c_{SDS} = 300 and 600 mM solutions. The nanoscopic topography reveals extended flat areas of uniform thickness with a few non-flat features. Zhang *et al.*[19, 22, 30, 31] introduced the IDIOM protocols and were the first to outline such thickness maps for foam films composed of c_{SDS} < 100 mM. In a previous study,[20] Ochoa *et al.* extended such measurements for $c_{SDS} \leq 250$ mM. However, there are no reports or studies of the nanotopography for foam films with c_{SDS} > 250 mM, and in addition to stepwise thinning, the thickness maps reveal the presence of coexisting thick-thin regions.

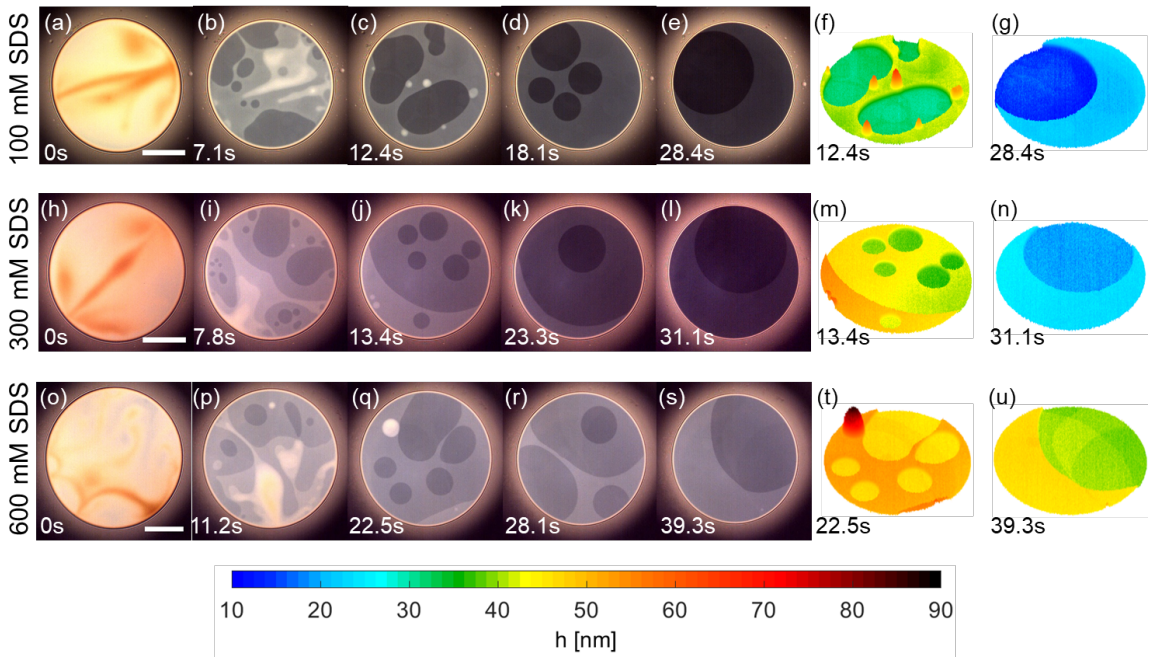

Figure 2. Coexisting thick-thin regions shown in grey scale images and maps of nanoscopic topography obtained using IDIOM protocols. Brightness-enhanced snapshots ((a) to (e) for 100 mM, (h) to (i) for 300 mM, and (o) to (s) for 600 mM reveal the presence of thick-thin regions, manifested as multiple coexisting shades of gray. We refer to nearly circular thinner and darker regions as domains and occasional relatively brighter and thicker circular spots as mesas for c_{SDS} = 100 mM. The scale bar corresponds to 100 μm. The thickness maps ((f) and (g) for 100 mM, (m) and (n) for 300 mM, and (t) and (u) for 600 mM), correspond to the third and fifth snapshots of each row. In addition to the coexisting thick-thin flat regions, non-flat features like mesas are revealed in thickness maps. The spectrum of colors in the nm scale corresponds to the indicated range of thicknesses.

In Figure 2, the snapshots labeled t = 0 s correspond to the maximum intensity of red-wavelength light captured by the high-speed camera during each experiment. The snapshots after time t = 0 s show multiple coexisting shades of gray (domains) corresponding to different thickness-dependent interference intensities. For films of thickness h < 100 nm, a darker shade indicates a thinner region; thus, each montage shows that the average film thickness decreases as time progresses. The times shown in Figures 2e, 2l, and 2s correspond to the last domain that nucleated in the film during the experiment and increased from t = 28.4 s to t = 39.3 s between c_{SDS} = 100 and 600 mM, respectively, indicating longer experimental drainage times as c_{SDS} increased. Moreover, while the film thickness decreased, the nucleated domain number decreased from roughly 20 at t = 7.8 s to only 1 at t = 31.1 s for c_{SDS} = 300 mM (see Figure 2I and 2l). The domains with different shades of gray correspond to distinct metastable thicknesses, which have a quantized thickness difference $h_i - h_{i\text{-}1}$ equal to the step-size. Expanding domains coalesced with each other and the Plateau border, as shown in the supplementary video, and in an instance shown in Figure 2q (and the h-map in Figure 2t) for concentration c_{SDS} = 600 mM.

The snapshot in Figure 2c shows bright white spots at the moving front between expanding domains and the surrounding thicker film. Although these white spots appear to have rounded peaks in the thickness map, the corresponding thickness map included in Figure 2f reveals shape is tortilla-like. We termed them *mesas* for sharing similarities to the topographical features of a plateau or a tableland. The diameter of mesas is roughly three orders of magnitude larger (in microns) than their average thickness (in nm).[22, 30, 31] The size and morphology of mesas on surfactant films varied with time and c_{SDS}. Mesa observed for c_{SDS} = 600 mM, in Figure 2q and its corresponding thickness map has a diameter and thickness greater than that of the individual mesas shown for c_{SDS} = 100 mM. Lastly, the thickness map in Figure 2u for c_{SDS} = 600 mM shows an

expanding domain with multiple shades of green that are separated by edges and vertices, in contrast with smooth and nearly circular, expanding domain boundaries observed around domains in lower c_{SDS} films.[22, 30, 31]

The coexisting thick-thin regions and rich nanotopography displayed in stratified micellar films (see Figure 2 for example) arise due to the interplay of capillary pressure P_c and a thickness-dependent disjoining pressure, $\Pi(h)$, primarily influenced by supramolecular oscillatory structural contribution, $\Pi_{OS}(h)$ arising due to intermicellar structuring under confinement and intermicellar interactions.[15, 17, 22, 30, 31] In these experiments carried out for salt-free micellar SDS solutions, the Laplace pressure is kept nearly constant by matching the film and cell size. However, the $\Pi(h)$ changes in amplitude and periodicity with SDS concentration, leading to the observed changes in step size and number of steps, as well as the formation and growth of thinner, darker domains shown in Figure 1b. Our theoretical model based on a thin film equation amended with $\Pi_{os}(h)$ captures [22, 30-33] the shape and shape evolution of nanotopographical features for the salt-free case. Thus, an interplay of structural disjoining pressure and capillary pressure sculpts the nanotopography of stratified foam films, in analogy with how nanoscopic features in polymer films undergoing dewetting provide evidence for the role of disjoining pressure.[45, 76, 77] Therefore, the nanotopographical maps created using the IDIOM protocols shown in Figure 2 must be considered as the markers of the interactions and microstructure that determine and influence the amplitude, periodicity, and decay length of $\Pi_{os}(h)$, and the stability and lifetime of foam films.

Effect of SDS concentration on step size, flat film thicknesses, h_i and the number of layers

Figure 3a shows all the step size values reported in the literature for salt-free aqueous SDS solutions.[16, 17, 25, 26, 28, 29, 42, 78] The published claims about step size following as inverse cubic law or $\Delta h \sim c_{SDS}^{-1/3}$ were based on the values measured over a narrower concentration range (c < 100

mM) using Scheludko cell and freely draining horizontal films. Figure 3a excludes the step size vs concentration datasets obtained using IDIOM protocols for $c/CMC < 30$.[19-22, 30-34] However, we included an additional dataset by Krichevsky and Stavans[25] made by dipping and drawing 0.3 x 2.0 cm^2 PVC frames into SDS solutions formulated in a mixture of deionized water and 4 wt.% glycerol. We find that the dashed line extrapolating $\Delta h \sim c_{\mathrm{SDS}}^{-1/3}$ captures the concentration-dependent variation observed implying that despite the presence of glycerol and a much larger span of the foam film (possibly lower capillary pressure), a similar stratification process underlies this drainage process. Figure 3b shows the corresponding step size variation with concentration for an extended range of SDS concentrations acquired using IDIOM protocols. The value of Δh shown in Figure 3b decreased from 14 nm to 6 nm as c_{SDS} increased from c_{SDS} = 30 to 600 mM. Even if we consider the values of step size measured by Krichevsky and Stavans[25] for five concentrations in the range, c_{SDS} = 150 to 600 mM, the extensive measurements shown in Figure 3 are quite remarkable and imply that the measured values follow the inverse cubic relationship or $\Delta h \sim c_{\mathrm{SDS}}^{-1/3}$ included as a dashed line.

The data shown in Figure 3b for salt-free SDS solutions was acquired using the same Scheludko cell with comparable Laplace pressure acting on the plane parallel films for each sample. No salt or electrolyte is added to the SDS solutions as salt addition changes CMC, micelle size, and number density and reduces amplitude, periodicity decay length of supramolecular contribution to disjoining pressure, thereby resulting in smaller step size, formation of isolated mesas, and diminished number of steps during thinning process.[33, 34] The inverse cubic scaling suggest that the step-size could be set by the number density of micelles. However, as micelles can change shape and size with surfactant concentration, as evaluation of their size, shape and interactions is needed, and carried out using x-ray scattering, as discussed in the next section.

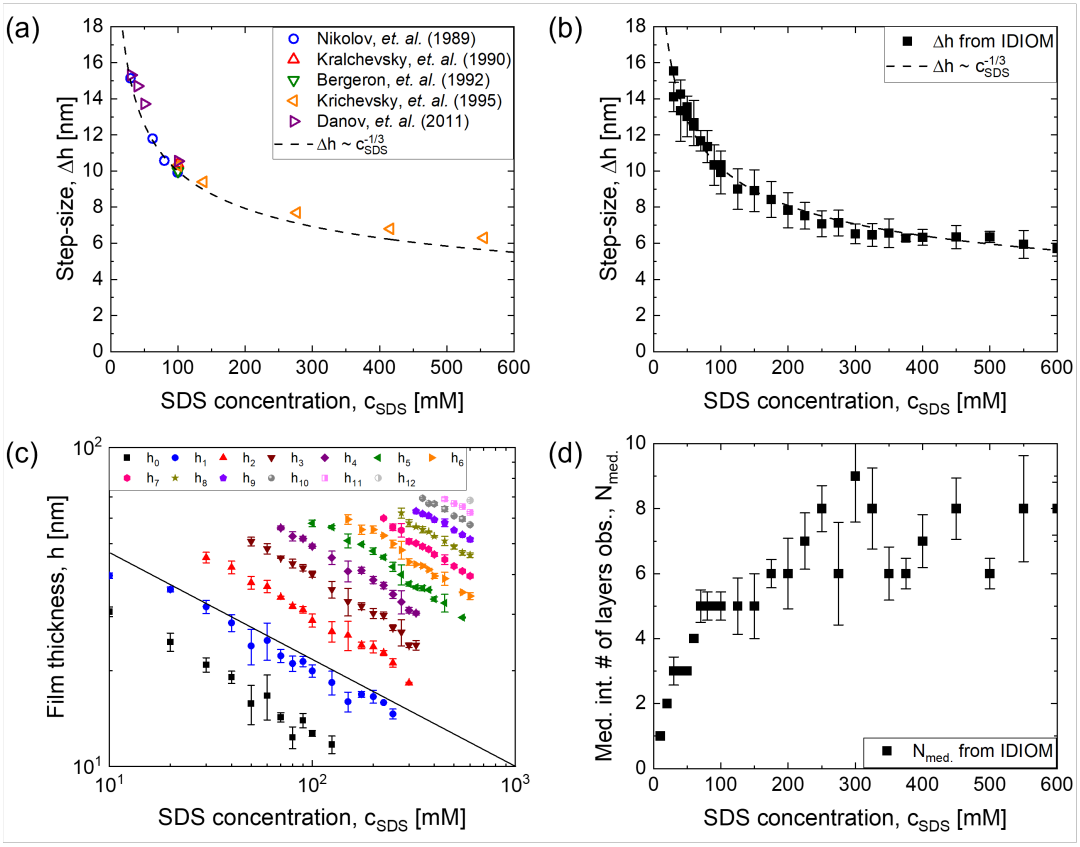

Figure 3. Step size, Δh and metastable flat film thicknesses, h_i as a function of SDS concentration c_{SDS}. (a) Step size, Δh *vs.* concentration plot includes all the published experimental data for salt-free stratifying micellar SDS foam films (excludes datasets obtained using IDIOM protocols by coauthors). **(b)** Step size, Δh vs. concentration datasets obtained using the IDIOM protocols show that the inverse cubic dependence captures the variation in step size for an extended range of SDS concentrations. (c) Metastable thickness h_i as a function of SDS concentration shown on a log-log graph to illustrate the inverse cubic root power law $h_i \sim c_{SDS}^{-1/3}$. (d) The number of layers observed in the Scheludko cell (for P_c = 90 Pa).

The metastable thickness, h_i as a function of SDS concentration plots (obtained from h vs. t plots) are shown in the log-log graphs in Figure 3c. Such plots of h_i as a function of surfactant concentration are not available in published literature, except in an early paper by Bruill and Lyklema[23] showing $h_i \sim c_{SDS}^{-1/3}$. The concentration dependence is analogous to $\Delta h \sim c_{SDS}^{-1/3}$, even though h_i includes contributions from supramolecular structural and shorter-range forces (including DLVO and solvation).[33, 47] The transition from one metastable thickness to the next

during stratification can be considered a nucleation and growth process, and the activation energy for this transition rises as a film gets thinner and micellar concentration increases. Therefore, the lowest step or film thickness achieved depends on the surfactant concentration for a fixed Laplace pressure. Data shown in Figure 3c highlights that with an increase in c_{SDS}, the index number of the minimum metastable thickness h_i increases. As the layer number in Figure 3c is chosen by accounting for the role played by increased amplitude of disjoining pressure, the index runs up to 12. The maximum h_i saturates around a film thickness of 70 nm. Correspondingly, Figure 3d shows the median integer number of layers observed, $N_{med.}$ and the number seems to plateau close to 8 for higher concentrations, as our experiments are carried out under relatively low, fixed Laplace pressure (90 Pa). Higher Laplace pressures can be obtained by using porous plate cells[16, 17, 30, 79-81] as long as pores are small and adequate care is taken for removing impurities or by employing set-ups like the bike-wheel set-up that enables more precise control over withdrawal rate (rather than use self-draining) and ambient pressure around the film[82-84].

Small-Angle X-ray Scattering (SAXS) of Micellar SDS Solutions

Small-angle X-ray scattering (SAXS) was employed to probe the micelle size and shape and intermicellar interactions for 100 mM ≤ c_{SDS} ≤ 600 mM (~12 ≤ c_{SDS}/CMC < 75). The one-dimensional SAXS intensities $I(q)$, as a function of wave vector q, for a series of aqueous SDS solutions are shown in Figure 4a. The SAXS spectra for a dispersion of scatterers can be described as a product of form and structure factor, $I(q) \sim \phi P(q) S(q)$ corresponding to the scattering contributions from individual micelles and the spatial correlations between them. The intermediate-q peak, corresponding to smaller length scales, signifies the $P(q)$ contributions and reveals information about the shape and size of the SDS self-assemblies. In contrast, the low-q peak, corresponding to larger length scales, signifies the $S(q)$ contributions. The SAXS spectra for

SDS solutions at low SDS concentrations (c_{SDS} < 300 mM) exhibit distinct peaks in the low and intermediate q range (q < 0.9 nm^{-1} and 1.5 nm^{-1} < q < 2.5 nm^{-1}, respectively) separated by a sharp valley. This unique valley near q = 0.9 nm^{-1} is contributed by the $P(q)$ emerging from differences in the scattering length density between the micelle core, the micelle shell, and the solvent.

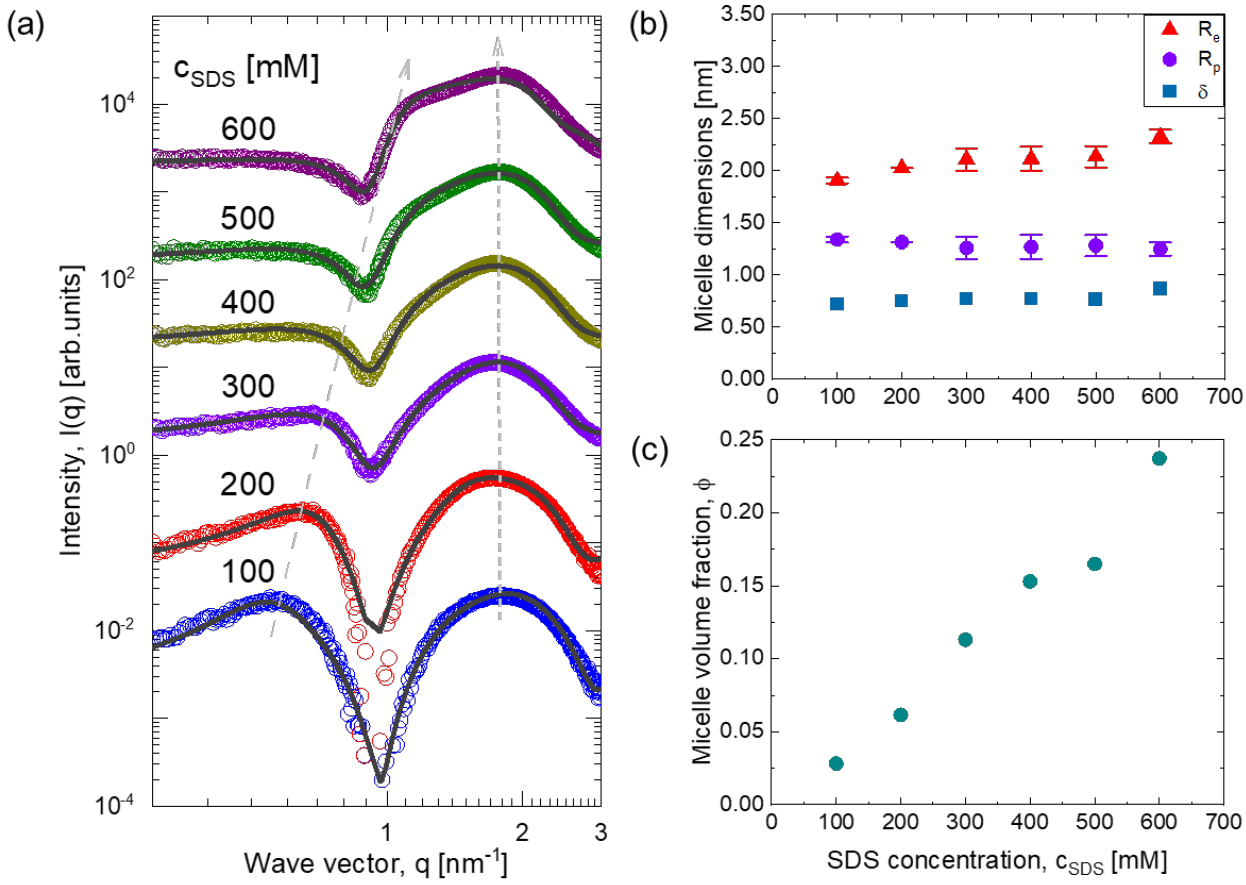

Figure 4. Small Angle X-Ray Scattering (SAXS) measurements for c_{SDS} = 100 – 600 mM solutions. (a) SAXS intensity I as a function of wavevector q are shown in open circles. The solid lines are fits that correspond to the form factor model of oblate ellipsoids and structure factor models of Hayter-Penfold, respectively. The scattering profiles have been shifted vertically for clarity. Dashed lines indicate track structure and form factor peaks. **(b)** Micelle dimensions as a function of SDS concentration: core radii along the major axis R_e, core radii along the minor axis R_p, and shell thickness δ. **(c)** Micelle volume fraction ϕ as a function of SDS concentration.

The dominant structure factor $S(q)$ peaks appear at q ~ 0.6 nm^{-1} for a solution with c_{SDS} = 100 mM and shifts to higher q values with increasing c_{SDS} till 300 mM, indicating decreasing

intermicellar distance d suggested by the relationship $d = 2\pi/q^*$, where q^* is the wave vector position of the primary $S(q)$ peak. For SDS solutions with c_{SDS} = 400 - 600 mM, $I(q)$ continues to demonstrate a $P(q)$ peak in the region 1.5 nm^{-1} < q < 2.5 nm^{-1}, with the $P(q)$ peak position remaining nearly independent of c_{SDS}, indicating little variation in the characteristics of individual micelles with increasing c_{SDS} from 100 mM to 600 mM. At the same time, there are no noticeable peaks in the q < 1 nm^{-1} region where $I(q)$ remains nearly flat. This infers that the rightward shifting $S(q)$ peak begins to overlap with the $P(q)$ valley at q ~ 1 nm^{-1}, consistent with the shifting of $S(q)$ peaks to higher q values with increasing c_{SDS}. Moreover, a bulge appears near q ~ 1.2 nm^{-1} for c_{SDS} = 400 - 600 mM, which likely indicates interference between the shifting $S(q)$ peak with the $P(q)$ peaks. Beyond 500 mM the analysis with the Hayter-Penfold model becomes trickier, and a well-defined second peak appears for aqueous SDS solutions in structure factor beyond 20 wt.% (or c/CMC >83).[69]

The solid lines shown in Figure 4a are fit to the scattered intensity profiles and rely on oblate core-shell ellipsoid form factor[7, 85] and Hayter-Penfold structure factor models[86-88] based on rescaled mean spherical approximation (RMSA) for particles interacting with screened Coulomb repulsion. For the entire range, c_{SDS} = 100 – 500 mM, the fits reveal that micelle size remains nearly constant with an increase in SDS concentration. The oblate core-shell ellipsoid form factor model fits indicate that the micelle core minor axis radius is R_p = 1.3 nm, the micelle shell thickness is δ = 0.75 nm, and that both are independent of SDS concentration in the range 100 ≤ c_{SDS} ≤ 500 mM, while the micelle core major axis radius slightly increases from R_e = 1.9 to 2.1 nm for c_{SDS} = 100 – 500 mM, as shown in Figure 4b. The micelle core minor axis radius R_p values for c_{SDS} = 100 and 200 mM agree with the values of micelle core radius obtained by Bezzobotnov *et al.*[89] using small angle neutron scattering (SANS). The total micelle radii (R_p or R_e + δ) values for c_{SDS} = 300

mM nearly agree with those obtained by Putra and Ikram using SANS[90]. The $R_p + \delta$ values for $c_{SDS} \leq 500$ mM agree with the total micelle radii calculated by Itri and Amaral using SANS,[69] and the $R_p + \delta$ values for $c_{SDS} = 300$ and 500 mM with values reported by Gubaidullin *et al.* using SAXS[91]. The size and shape of SDS micelles and intermicellar distances at matched concentrations also correspond to the few values reported in the 1980s by Hayter, Penfold, Cabane, Zemb, Shen, Amaral, and others in the classical papers.[73, 86-88, 92-94] The Hayter-Penfold structure factor model fits indicate a monotonic increase in micelle volume fraction from $\phi = 0.025$ to 0.25 for $c_{SDS} = 100$ – 600 mM, as shown in Figure 4c. The linearly increasing volume fraction, decreasing intermicellar distance, and variation in micelle size and shape with SDS concentration influence the supramolecular oscillatory disjoining pressure in stratifying thin films. In a subsequent section, we compare the intermicellar distance to calculated values of step size, Δh, as a function of SDS concentration.

Concentration-Dependent Variation in Viscosity of SDS solutions

We measure concentration-dependent variation in steady shear viscosity next to as it is well established that substantial increase in viscosity occurs as wormlike micelles form on increasing surfactant concentration and such micellar solutions display rate-dependent steady shear viscosity and viscoelastic response (Linear LVE is often Maxwellian).[95, 96] Steady shear viscosity measurements with double-gap Couette geometry show that the viscosity of aqueous solutions is within a factor of two of water viscosity for $c < 250$ mM. The relative viscosity is less than four times the solvent viscosity for 600mM solutions and the shear viscosity is rate independent. These observations are consistent with findings from x-ray scattering studies (shown in Figure 3) that the micelles dimensions seems to vary only marginally for this concentration range. Figure 5a plots the relative viscosity aqueous SDS solutions measured in this investigation along with the

previously reported values, and there are no dramatic viscosity enhancements that could be attributed to changes in micellar shape and size. The scattering and rheology results are thus consistent with each other. We included relatively unknown data from Ito et al.[97] (the paper written in Japanese has only four citations in fifty-five years!). On excluding the Ito el al. study,[97] only few datapoints remain, with hardly any for c >150 mM, and there is considerable mismatch between the reported values. Our viscosity values closely agree with the previous studies,[97-99] with the exception of the values reported by Chari et al.[100] Given the significant lack of published data on shear viscosity of aqueous SDS solutions and the stark differences between the few published values, we determined a careful measurements of viscosity over an extended range of concentrations are necessary.

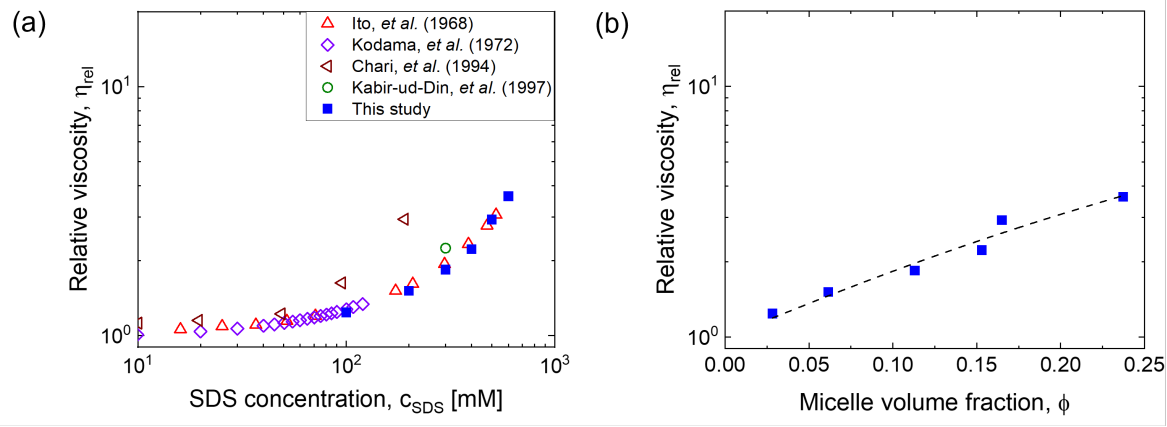

Figure 5. The relative viscosity of aqueous SDS solutions obtained by scaling micellar solution viscosity with the viscosity of water (solvent). (a) Viscosity values reported in the literature contrasted against the values measured here. The data is shown on a log-log scale, to emphasize that for concentrations below 250 mM, the viscosity is within a factor of 2 of solvent viscosity. (b) Relative viscosity values measured using double gap geometry on a torsional rheometer for the SDS solutions used in stratification studies.

Since this increase in viscosity with SDS concentration occurs due to an increase in number density of charged micelles, in Figure 5b we plotted the relative viscosity values as a function of micelle volume fraction (values determined from the analysis of X-ray scattering) for SDS

concentration in the range of 100 mM-600 mM. Here we chose to show data on a semilog plot to emphasize that the viscosity increases nonlinearly with concentration. The behavior can be captured by an exponential function or a second-order polynomial. The scattering and rheology studies show micelles of nearly similar size and shape developing stronger correlations due to the influence of an increase in their number density. For a nanoparticle system, the concentration dependence of viscosity can be modeled by simply accounting for number density and screened electrostatic interactions.[101] However, for these micellar solutions, the aggregation number, an effective charge per headgroup of a unimer in solution, and those embedded in micelles, and the micelle shape are all perturbed with an increased amount of surfactant.[7, 66, 69, 71, 73, 94]

Effect of SDS concentration on the step size and intermicellar distances

The scattering data analysis reveals dimensions related to micelle size and shape that are determined from the oblate ellipsoids form factor, $P(q)$ and an additional length scale corresponding to the peak position for structure factor, $S(q)$. The location of this peak provides a measurement of the concentration-dependent variation in intermicellar interactions related to the intermicellar distance, and the structure factor chosen here is built assuming the dominant role of screened Coloumb interactions between micelles. Figure 6a shows the structure factor $S(q)$ as a function of wave vector q for six SDS concentrations. Each profile corresponds to the Hayter-Penfold model fits of the $I(q)$ data. Each $S(q)$ profile possesses two peaks, one (primary peak) at values $q < 1.2$ nm^{-1} and one at values $q > 1.2$ nm^{-1}. The intermicellar distance d is correlated with the inverse of the position of the primary $S(q)$ peak (at q^*) as $d = 2\pi/q^*$. The value of q^* increases from $c_{SDS} = 100$ to 600 mM.

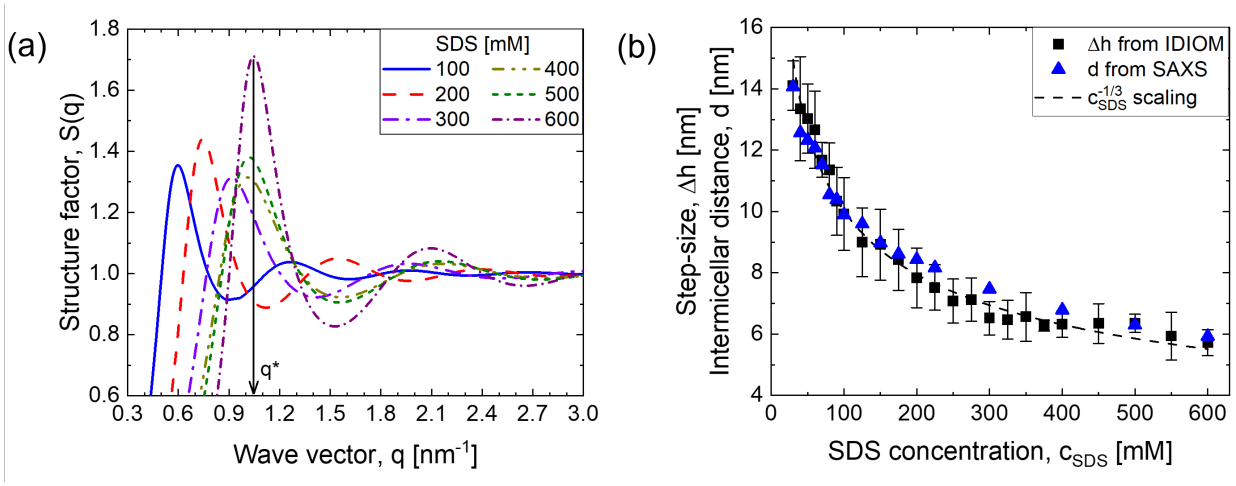

Figure 6. Structure factor, $S(q)$, intermicellar distance, d, and step-size, Δh of aqueous SDS solutions. (a) Structure factor $S(q)$ as a function of the wave vector q obtained using the Hayter-Penfold model for the six SDS concentrations. The peak position q^* shifts to a larger value (smaller length scale with an increase in SDS concentration. **(b)** Step size, Δh measured using IDIOM protocols (with the corresponding error bar) and intermicellar distance measured using SAXS are compared as a function of SDS concentration. The dashed line denotes the inverse cubic root power law $\Delta h \sim c_{SDS}^{-1/3}$.

Figure 6b shows a plot of intermicellar distance d as a function of SDS concentration, which was measured by using SAXS protocols, and includes the step-size $\Delta h = h_{i+1} - h_i$ (except any $h_1 - h_0$), obtained using thickness-time plots for stratifying foam films. Complementary scattering and foam drainage studies here show that the concentration-dependent variation in intermicellar distances and interactions for c/CMC <75 follow the trends well known from the extensive micellar SDS foam film stratification studies that were typically restricted to c/CMC < 12. In addition to showing comparable magnitude, like step size, intermicellar distance displays a concentration-dependent variation of the inverse cubic root law or $d \sim c_{SDS}^{-1/3}$. The screened Coulomb interactions among ionic micelles captured by the Hayter-Penfold model that determine intermicellar distance and microstructure in bulk solutions also set the periodicity of the oscillatory structural disjoining pressure that influences foam film stability and topography.

In 1990s, Radke and coworkers[16, 17, 55, 56] invoked a hydrodynamic model to describe domain expansion during stratification and used density functional theory to characterize structure and viscosity in thin films. The hydrodynamic model predicted nanoridge formation experimental validation of model was not carried out. An alternative mechanism proposed confined micelles form an "ordered colloidal crystal" with density, ordering, and viscosity distinct from the bulk and required neither thin film equation nor ridge formation. Our previous studies detail the relative merits of two mechanisms and describe stratification kinetics and shape evolution of nanotopographical features quantitatively using a thin film equation amended with a disjoining pressure dominated by $\Pi_{os}(h)$ by using bulk viscosity[19, 22, 30-33, 36]. Though our previous comparisons of scattering and stratification were restricted low volume fractions (< 10%), with step size or intermicellar distance significantly larger than real or effective micelle size, the comparison here are made upto much higher concentration (600 mM or ϕ~25%), and similar form and structure factors govern the behavior. Larger Debye length at low volume fraction and reduced Debye length on increasing surfactant concentration without significant change in micelle size imply that effective volume fraction remains below close packing, and symmetry breaking at the interface drives structuring within films. Stratification of micellar foam films are thus a subset of studies that describe structuring of macroions near walls, created by larger particles, drops, bubbles, or surfaces of SFA or CP-AFM.[2, 25, 27, 41, 54-64, 102] (see the reviews for a recent, comprehensive summary[53]).

Even though here we focus on stratifying micellar foam films, similar confinement-induced layering of supramolecular structures leads to stratification in many thin films of soft matter. including nanoparticles,[15, 26, 42, 65] lipid layers,[79, 103] polyelectrolyte-surfactant complexes,[41, 43] and liquid crystalline assemblies.[104] In all cases, the symmetry-breaking at the interface and

interparticle interactions that lead to structuring and layering contributes a $\Pi_{os}(h)$ that can counterbalance capillary pressure, P_c at multiple thicknesses manifested as coexisting thick-thin regions. However, in-plane correlations and differences in the shape, size and concentration-dependent behavior of supramolecular structures provide a rich tapestry of distinct observations. For example, the formation of nanoridges and mesas is not observed for stratifying liquid crystalline films, and step size for nanoparticle dispersions is not dependent or influenced by salt concentration. Many open questions remain regarding how stratification behavior would change if surfactant concentrations are increased substantially, creating wormlike micelles and liquid crystalline phases. The substantial increase in the concentration range from typical c/CMC < 12 to c/CMC <75 explored here represents a critical step in that exploration.

CONCLUSIONS

We show that micellar foam films formed using aqueous SDS solutions exhibit drainage via stratification for concentration as high as 600 mM (c/CMC < 75). The analysis of drainage in single foam films created in Scheludko cells reveals that step size exhibits the inverse cubic root scaling with surfactant concentration for the entire concentration range examined. Using IDIOM protocols we observe the co-existence of flat thick-thin regions that differ in thickness by step size, and observe the non-flat features like mesas that spontanously form during drainage. In addition to step size, the individual thicknesses observed during step wise thinning are also included here, and show the inverse cubic power law dependence on surfactant concentration, $h_i \sim c_{SDS}^{-1/3}$. We examine the influence of increasing surfactant concentration on micellar dimensions and intermicellar interactions using small-angle X-ray scattering, by using Hayter-Penfold model to describe the structure factor. We contrast intermicellar distance in bulk (measured by scattering) and the step-size of stratifying foam films to find both have similar magnitude and display inverse

cubic power law dependence on concentration or $\Delta h = d \sim c^{-1/3}$. Step-size and intermicellar distance are correlated with the periodicity of supramolecular oscillatory structural forces, as well as with the inverse q^* position of the primary $S(q)$ peak from scattering experiments. Moreover, the number of layers observed in the stratifying foam film increases as a function of SDS concentration, correlating with the magnitude and decay length of supramolecular oscillatory structural forces as well as that of the structure factor profile.

The observations of stepwise thinning, the coexistence of thick-thin regions, and nanotopography attest to the role played by supramolecular oscillatory structural disjoining pressure that arises due to the interplay of the confinement by surfactant-rich interfaces and electrostatic intermicellar interactions. In addition to observing, drainage via stratification for a wider range of concentrations than reported and understood before, we present a detailed portrait of how the micelle size and shape, and volume fraction vary with an increase in SDS concentration and influence macroscopic properties like foam film stability and drainage. We infer that foam film drainage, viscosity, and scattering behavior (dependent on the shape, size, interactions and structuring) of micellar solutions over an extended concentration range are consistent with hydrodynamic mechanism for drainage via stratification with the role of a $\Pi_{os}(h)$ that increases in amplitude and decreases in periodicity with the increase in micellar number density. We anticipate that the range of concentrations for which step size and intermicellar distance display the inverse cubic root scaling on surfactant concentration is sensitive to the physicochemical properties of the surfactant unimers and micelles. Future studies can explore the connection between the phase behavior of surfactants, drainage kinetics in single foam films and how choice of surfactant influence the range of concentrations for which intermicellar distance and step size are comparable.

REFERENCES

1. P. G. de Gennes, F. Brochard-Wyart and D. Quéré, *Capillarity and Wetting Phenomena: Drops, Bubbles, Pearls, Waves*, Springer-Verlag, New York, 2004.
2. J. N. Israelachvili, *Intermolecular and Surface Forces*, Elsevier, Waltham, MA, 3rd edn., 2011.
3. I. Cantat, S. Cohen-Addad, F. Elias, F. Graner, R. Höhler and O. Pitois, *Foams: Structure and Dynamics*, Oxford University Press, Oxford, 2013.
4. P. Kekicheff, C. Grabielle-Madelmont and M. Ollivon, *J. Colloid Interface Sci.*, 1989, **131**, 112-132.
5. B. Hammouda, *Journal of research of the National Institute of Standards and Technology*, 2013, **118**, 151.
6. X. Tang, P. H. Koenig and R. G. Larson, *The Journal of Physical Chemistry B*, 2014, **118**, 3864-3880.
7. K. Schäfer, H. B. Kolli, M. Killingmoe Christensen, S. L. Bore, G. Diezemann, J. Gauss, G. Milano, R. Lund and M. Cascella, *Angew. Chem.*, 2020, **132**, 18750-18757.
8. F. H. Quina, P. M. Nassar, J. B. Bonilha and B. L. Bales, *The Journal of Physical Chemistry*, 1995, **99**, 17028-17031.
9. C. Ochoa, C. Xu, C. D. M. Narváez, W. Yang, Y. Zhang and V. Sharma, *Soft Matter*, 2021, **17**, 8915-8924.
10. R. A. Duncan, *Industrial & Engineering Chemistry*, 1934, **26**, 24-26.
11. A. R. Padgett and E. F. Degering, *Industrial & Engineering Chemistry*, 1940, **32**, 204-208.
12. C. A. M. Bondi, J. L. Marks, L. B. Wroblewski, H. S. Raatikainen, S. R. Lenox and K. E. Gebhardt, *Environmental health insights*, 2015, **9**, EHI. S31765.
13. S. Bom, J. Jorge, H. M. Ribeiro and J. Marto, *Journal of Cleaner Production*, 2019, **225**, 270-290.
14. A. D. Nikolov and D. T. Wasan, *J. Colloid Interface Sci.*, 1989, **133**, 1-12.
15. A. D. Nikolov, D. T. Wasan, P. A. Kralchevsky and I. B. Ivanov, Kyoto, Japan, 1988.
16. V. Bergeron, A. I. Jimenez-Laguna and C. J. Radke, *Langmuir*, 1992, **8**, 3027-3032.
17. V. Bergeron and C. J. Radke, *Langmuir*, 1992, **8**, 3020-3026.
18. P. Heinig, C. M. Beltran and D. Langevin, *Phys. Rev. E.*, 2006, **73**, 051607-051601-051608.
19. Y. Zhang and V. Sharma, *Soft Matter*, 2015, **11**, 4408-4417.
20. C. Ochoa, S. Gao, S. Srivastava and V. Sharma, *Proc. Natl. Acad. Sci. U.S.A.*, 2021, **118**, e2024805118.
21. C. Xu, C. D. V. Martínez Narváez, P. Kotwis and V. Sharma, *Langmuir*, 2023, **39**, 5761–5770.
22. Y. Zhang, S. Yilixiati, C. Pearsall and V. Sharma, *ACS Nano*, 2016, **10**, 4678-4683.
23. H. G. Bruil and J. Lyklema, *Nature Physical Science*, 1971, **233**, 19.
24. A. A. Sonin and D. Langevin, *EPL (Europhysics Letters)*, 1993, **22**, 271.
25. O. Krichevsky and J. Stavans, *Phys. Rev. Lett.*, 1995, **74**, 2752.
26. D. T. Wasan and A. D. Nikolov, *Curr. Opin. Colloid Interface Sci.*, 2008, **13**, 128-133.

27. S. E. Anachkov, K. D. Danov, E. S. Basheva, P. A. Kralchevsky and K. P. Ananthapadmanabhan, *Adv. Colloid Interface Sci.*, 2012, **183**, 55-67.
28. J. Lee, A. Nikolov and D. Wasan, *J. Colloid Interface Sci.*, 2017, **496**, 60-65.
29. J. Lee, A. D. Nikolov and D. T. Wasan, *J. Colloid Interface Sci.*, 2017, **487**, 217-222.
30. Y. Zhang and V. Sharma, *Langmuir*, 2018, **34**, 1208-1217.
31. Y. Zhang and V. Sharma, *Langmuir*, 2018, **34**, 7922–7931.
32. S. Yilixiati, E. Wojcik, Y. Zhang and V. Sharma, *Mol. Sys. Des. Eng.*, 2019, **4**, 626-638.
33. S. Yilixiati, R. Rafiq, Y. Zhang and V. Sharma, *ACS Nano*, 2018, **12**, 1050-1061.
34. S. Gao, C. Ochoa, V. Sharma and S. Srivastava, *Langmuir*, 2022, **38**, 11003-11014.
35. L. Hassan, C. Xu, M. Boehm, S. K. Baier and V. Sharma, *Langmuir*, 2023, **39**, 6102-6112.
36. S. I. Kemal, C. A. U. Ortiz and V. Sharma, *Mol. Sys. Des. Eng.*, 2021, **6**, 520-533.
37. C. V. Boys, *Soap Bubbles: Their Colours and the Forces Which Mold Them*, Society for Promoting Christian Knowledge, London, 1912.
38. K. J. Mysels, S. Frankel and K. Shinoda, *Soap films: Studies of their Thinning and a Bibliography*, Pergamon Press, 1959.
39. G. Gochev, D. Platikanov and R. Miller, *Adv. Colloid Interface Sci.*, 2016, **233**, 115-125.
40. M. Born and E. Wolf, *Principles of optics: electromagnetic theory of propagation, interference and diffraction of light*, Elsevier, 2013.
41. R. v. Klitzing, E. Thormann, T. Nylander, D. Langevin and C. Stubenrauch, *Adv. Colloid Interface Sci.*, 2010, **155**, 19-31.
42. D. T. Wasan, A. D. Nikolov, P. A. Kralchevsky and I. B. Ivanov, *Colloids Surf.*, 1992, **67**, 139-145.
43. C. M. Beltrán and D. Langevin, *Phys. Rev. Lett.*, 2005, **94**, 217803.
44. C. J. Radke, *J. Colloid Interface Sci.*, 2015, **449**, 462-479.
45. S. Kalliadasis and U. Thiele, *Thin Films of Soft Matter*, SpringerWien NewYork, 2007.
46. A. Sheludko, *Adv. Colloid Interface Sci.*, 1967, **1**, 391-464.
47. V. Bergeron, *J. Phys.: Condens. Matter*, 1999, **11**, R215-R238.
48. D. L. Weaire and S. Hutzler, *The Physics of Foams*, Oxford University Press, Oxford, 1999.
49. B. V. Derjaguin, N. V. Churaev and V. M. Muller, *Surface Forces*, Springer, New York, 1987.
50. J. Israelachvili and M. Ruths, *Langmuir*, 2013, **29**, 9605-9619.
51. D. Fennell Evans and H. Wennerström, *The Colloidal Domain: Where Physics, Chemistry, Biology, and Technology Meet*, Wiley-VCH: New York, 2nd edn., 1999.
52. P. A. Kralchevsky and N. D. Denkov, *Chem. Phys. Lett.*, 1995, **240**, 385-392.
53. M. Ludwig and R. von Klitzing, *Curr. Opin. Colloid Interface Sci.*, 2020.
54. M. Ludwig, M. U. Witt and R. von Klitzing, *Adv. Colloid Interface Sci.*, 2019, **269**, 270-276.
55. M. L. Pollard and C. J. Radke, *J. Chemical Physics*, 1994, **101**, 6979-6991.
56. M. L. Pollard and C. J. Radke, *AlChE J.*, 1996, **42**, 2005-2013.
57. O. Krichevsky and J. Stavans, *Phys. Rev. E.*, 1997, **55**, 7260.
58. A. Trokhymchuk and D. Henderson, *Curr. Opin. Colloid Interface Sci.*, 2015, **20**, 32-38.
59. A. Tulpar, P. R. Van Tassel and J. Y. Walz, *Langmuir*, 2006, **22**, 2876-2883.
60. Y. Zeng, S. Schön and R. von Klitzing, *J. Colloid Interface Sci.*, 2015, **449**, 522-529.
61. Y. Zeng and R. von Klitzing, *Soft Matter*, 2011, **7**, 5329-5338.
62. Y. Zeng and R. von Klitzing, *Journal of Physics-Condensed Matter*, 2012, **24**.

63. S. H. L. Klapp, S. Grandner, Y. Zeng and R. von Klitzing, *J. Phys.: Condens. Matter*, 2008, **20**.
64. S. H. L. Klapp, S. Grandner, Y. Zeng and R. von Klitzing, *Soft Matter*, 2010, **6**, 2330-2336.
65. E. S. Basheva, K. D. Danov and P. A. Kralchevsky, *Langmuir*, 1997, **13**, 4342-4348.
66. P. Kekicheff and B. Cabane, *Journal de Physique*, 1987, **48**, 1571-1583.
67. A. S. Rafique, S. Khodaparast, A. S. Poulos, W. N. Sharratt, E. S. Robles and J. T. Cabral, *Soft Matter*, 2020, **16**, 7835-7844.
68. Y. Chevalier and T. Zemb, *Rep. Prog. Phys.*, 1990, **53**, 279.
69. R. Itri and L. Q. Amaral, *J. Phys. Chem.*, 1990, **94**, 2198-2202.
70. J. A. Goshawk, D. M. Binding, D. B. Kell and R. Goodacre, *J. Rheol.*, 1998, **42**, 1537-1553.
71. E. Y. Sheu, C.-F. Wu, S.-H. Chen and L. Blum, *Phys. Rev. A*, 1985, **32**, 3807.
72. S. H. Chen, E. Y. Sheu, J. Kalus and H. Hoffman, *J. Appl. Crystallogr.*, 1988, **21**, 751-769.
73. R. Itri and L. Q. Amaral, *Phys. Rev. E.*, 1993, **47**, 2551.
74. D. Langevin and A. A. Sonin, *Adv. Colloid Interface Sci.*, 1994, **51**, 1-27.
75. C. D. V. Martínez Narváez, T. Mazur and V. Sharma, *Soft Matter*, 2021, **17**, 6116-6126.
76. R. Mukherjee and A. Sharma, *Soft Matter*, 2015, **11**, 8717-8740.
77. R. Seemann, S. Herminghaus and K. Jacobs, *Phys. Rev. Lett.*, 2001, **87**, 196101.
78. P. A. Kralchevsky, A. D. Nikolov, D. T. Wasan and I. B. Ivanov, *Langmuir*, 1990, **6**, 1180-1189.
79. Z. Lalchev, R. Todorov and D. Exerowa, *Curr. Opin. Colloid Interface Sci.*, 2008, **13**, 183-193.
80. D. Exerowa and A. Scheludko, *CR Acad Bulg Sci*, 1971, **24**, 47-50.
81. D. Exerowa and P. M. Kruglyakov, *Foam and Foam Films: Theory, Experiment, Application*, Elsevier, 1997.
82. E. Chatzigiannakis, N. Jaensson and J. Vermant, *Current Opinion in Colloid & Interface Science*, 2021, **53**, 101441.
83. E. Chatzigiannakis and J. Vermant, *Phys. Rev. Lett.*, 2020, **125**, 158001.
84. E. Chatzigiannakis and J. Vermant, *Soft Matter*, 2021, **17**, 4790-4803.
85. G. V. Jensen, R. Lund, J. Gummel, T. Narayanan and J. S. Pedersen, *Angew. Chem.*, 2014, **126**, 11708-11712.
86. J.-P. Hansen and J. B. Hayter, *Mol. Phys.*, 1982, **46**, 651-656.
87. J. B. Hayter and J. Penfold, *Mol. Phys.*, 1981, **42**, 109-118.
88. J. Hayter, B and J. Penfold, *Colloid. Polym. Sci.*, 1983, **261**, 1022-1030.
89. V. Y. Bezzobotnov, S. Borbely, L. Cser, B. Farago, I. A. Gladkih, Y. M. Ostanevich and S. Vass, *The Journal of Physical Chemistry*, 1988, **92**, 5738-5743.
90. E. G. R. Putra and A. Ikram, *Indonesian Journal of Chemistry*, 2010, **6**, 117-120.
91. A. T. Gubaidullin, I. A. Litvinov, A. I. Samigullina, O. S. Zueva, V. S. Rukhlov, B. Z. Idiyatullin and Y. F. Zuev, *Russ. Chem. Bull.*, 2016, **65**, 158-166.
92. B. Cabane, R. Duplessix and T. Zemb, *Journal De Physique*, 1985, **46**, 2161-2178.
93. T. Zemb and P. Charpin, *Journal de Physique*, 1985, **46**, 249-256.
94. R. Itri and L. Q. Amaral, *The Journal of Physical Chemistry*, 1991, **95**, 423-427.
95. C. A. Dreiss, *Soft matter*, 2007, **3**, 956-970.
96. J. P. Rothstein and H. Mohammadigoushki, *J. Non-Newtonian Fluid Mech.*, 2020, **285**, 104382.
97. T. Ito and H. Mizutani, *Journal of Japan Oil Chemists' Society*, 1968, **17**, 246-248.

98. M. Kodama and M. Miura, *Bull. Chem. Soc. Jpn.*, 1972, **45**, 2265-2269.
99. Kabir-ud-Din, S. L. David and S. Kumar, *J. Chem. Eng. Data*, 1997, **42**, 1224-1226.
100. K. Chari, B. Antalek, M. Y. Lin and S. K. Sinha, *J. Chem. Phys.*, 1994, **100**, 5294-5300.
101. W. B. Russel, D. A. Saville and W. R. Schowalter, *Colloidal Dispersions*, Cambridge University Press, Cambridge, 1989.
102. J. P. King, R. R. Dagastine, J. D. Berry and R. F. Tabor, *J. Colloid Interface Sci.*, 2023.
103. P. J. Beltramo and J. Vermant, *ACS Omega*, 2016, **1**, 363-370.
104. P. Oswald and P. Pieranski, *Smectic and Columnar Liquid Crystals: Concepts and Physical Properties Illustrated by Experiments*, Taylor and Francis, Boca Raton, FL, 2005.